

# Optics Letters

## Comparison of damage and ablation dynamics of multilayer dielectric films initiated by few-cycle pulses versus longer femtosecond pulses

NOAH TALISA,<sup>1</sup> ABDALLAH ALSHAFFEY,<sup>1</sup> MICHAEL TRIPEPI,<sup>1</sup> JACOB KREBS,<sup>1</sup>  
AARON DAVENPORT,<sup>4</sup> EMMETT RANDEL,<sup>4</sup> CARMEN S. MENONI,<sup>4</sup>  AND  
ENAM A. CHOWDHURY<sup>1,2,3,\*</sup>

<sup>1</sup>Department of Physics, The Ohio State University, 191 W Woodruff Ave., Columbus, Ohio 43210, USA

<sup>2</sup>Department of Material Science and Engineering, 2041 College Rd. N, Columbus, Ohio 43210, USA

<sup>3</sup>Department of Electrical and Computer Engineering, 2015 Neil Ave., Columbus, Ohio 43210, USA

<sup>4</sup>Electrical and Computer Engineering, Colorado State University, Fort Collins, Colorado 80523, USA

\*Corresponding author: chowdhury.24@osu.edu

Received 4 February 2020; revised 29 March 2020; accepted 30 March 2020; posted 30 March 2020 (Doc. ID 389650); published 1 May 2020

**The importance of high intensity few- to single-cycle laser pulses for applications such as intense isolated attosecond pulse generation is constantly growing, and with the breakdown of the monochromatic approximation in field ionization models, the few-cycle pulse (FCP) interaction with solids near the damage threshold has ushered a new paradigm of nonperturbative light-matter interaction. In this Letter, we systematically study and contrast how femtosecond laser-induced damage and ablation behaviors of SiO<sub>2</sub>/HfO<sub>2</sub>-based reflective multilayer dielectric thin film systems vary between FCP and 110 fs pulses. With time-resolved surface microscopy and *ex situ* analysis, we show that there are distinct differences in the interaction depending on the pulse duration, specifically in the “blister” morphology formation at lower fluences (damage) as well as in the dynamics of debris formation at higher fluences (ablation).** © 2020 Optical Society of America

<https://doi.org/10.1364/OL.389650>

The need for the generation of ultrabroadband, ultraintense single- to few-cycle laser pulses is ever-increasing as applications such as intense isolated attosecond pulse generation and laser-driven particle accelerators grow. This underlines the importance of the study of the high-intensity few-cycle pulse (FCP) laser-matter interaction. While the current understanding of femtosecond pulse laser-induced damage and ablation (LIDA) of dielectrics with pulse durations on the order of 100 fs has matured significantly over the past several decades, the FCP regime is still not well-understood, especially with the breakdown of the monochromatic approximation in the field ionization step for such broadband pulses. The typical assumptions of a static band structure fall apart for such strong fields that occur over only a few optical cycles [1], and the ensuing electron dynamics fall in an extremely nonequilibrium regime compared to the case with longer pulses. FCPs typically

exhibit bandwidth around  $\gtrsim 25\%$  of the carrier frequency, while  $\gtrsim 100$  fs pulses require  $\sim 1.5\%$  bandwidth. It implies that, first, the FCPs promote valence electrons to the conduction band at a higher rate (due to lower order of multiphoton processes for the high-frequency part of the broad FCP spectrum); second, the FCPs produce free electrons with higher kinetic energy compared to those produced by 110 fs pulses. The higher kinetic energy supports deeper electron penetration into samples and reduced electron-particle collision time. The reduced collision time drives the laser-generated free-carrier plasma faster to quasi-equilibrium and increases the rate of energy transfer to phonons. The increased rate of electron-phonon energy transfer supports reduced temperature of the laser-generated free-carrier plasma. Therefore, the FCPs are favorable for observing the transient processes at relatively lower fluence. However, also, the transient effects are observed over larger range of fluences due to the increased rate of energy transfer to the lattice via phonons. This is how in the case of femtosecond laser damage, whose dynamical evolution spans around 10 orders of magnitude [2], in time may retain the “memory” of the femtosecond impact long after the pulse has left. There have been few studies of the pulse duration dependence of LID of bulk dielectric materials down to the FCP regime [3,4], and even less LIDA of optical thin film dielectrics in that regime [5,6]. Similarly, although time-resolved surface microscopy (TRSM) has been widely used to study ultrafast laser melting and damage dynamics of bulk materials [7,8], there have been very few measurements of LIDA on optical thin films [5,6,9]. The study of the interaction between FCPs and optical thin film dielectric coatings directly impacts the development of high peak power FCP laser systems worldwide by facilitating the design of high damage threshold coatings in this regime. In this work, we extend the investigation of the FCP regime of LIDA of dielectrics using *ex situ* imaging and *in situ* TRSM to capture damage and ablation dynamics from 2 to 46 ns after an intense pulse interactions with

double- and quad-layer  $\text{HfO}_2/\text{SiO}_2$ -based coatings in a comparison between FCPs and 110 fs pulses (LP).

FCPs were generated using a home-built system [5] resulting in a full width half-maximum pulse duration of  $8 \pm 1$  fs, and a nominal central wavelength of 766 nm. Longer 110 fs duration pulses (LP) were achieved by evacuating the hollow-core fiber and adjusting the grating pulse compressor before the fiber. The pulses were focused onto the samples at an angle of incidence of  $45^\circ$  with  $p$  polarization and with an  $e^{-2}$  radius spot size of  $15 \mu\text{m}$ . In the TRSM setup, a low-intensity, frequency-doubled, time-delayed copy of the pump pulse acts as a probe pulse by illuminating the sample surface from the back and being collected by a microscope setup. Probe pulses have an approximate duration of 200 fs. Images of the damage process for each sample were captured at various times between  $\sim 2$  and  $\sim 46$  ns after the pump pulse arrived. After each shot, the sample was translated to a fresh site. Damage morphology was studied *ex situ* with a high power optical microscope as well as an atomic force microscope (AFM, Flex Axiom, Nanosurf). A more detailed description of the experimental setup can be found in Ref. [5].

The target thin film samples were deposited on fused silica substrates using ion beam sputtering (IBS) at conditions that result in ppm absorption loss at the design wavelength of 750 nm [10], and are designed for an angle of incidence of  $45^\circ$ . A single-layer  $\text{HfO}_2$  sample was made with quarter-wave optical thickness (QWOT, 97.6 nm). The double-layer sample comprises a QWOT layer of  $\text{HfO}_2$  underneath a half-wave optical thickness (HWOT) layer of  $\text{SiO}_2$  (299.1 nm), and the quad-layer sample has the same top two layers with two more QWOT layers underneath (similar to an alternating high/low index stack of QWOT layers). The double- and quad-layer samples were designed to maximize reflectance and minimize internal peak field at the design wavelength to enhance the damage threshold performance.

Figure 1 shows optical and AFM images of representative damage morphologies of the double-layer sample when irradiated with FCP. Similar morphologies were observed on the quad-layer sample, as well as for LP. For fluences just above the damage threshold fluence [Fig. 1(a)], which is the lowest fluence for which a permanent change is visible under confocal optical microscope with  $100\times$  magnification, a short ( $\sim 5$  nm tall) “bump” is formed. As the fluence is increased, a tall, sharp peak forms in the middle of the bump [Fig. 1(b)]. For larger fluences, this tall “blister” becomes more prominent, as shown in Fig. 1(c). Under the confocal optical microscope, the blister morphology exhibits concentric rings [Fig. 1(c), second column], which are most likely due to the variation of the interference condition of the thin film stack with the local height of the blister. This, along with the 3D AFM blister profiles versus fluence in Fig. 2, clearly indicates that at least the top of the  $\text{SiO}_2$  layer remains intact after either the  $\text{HfO}_2$  layer underneath has expanded due to nonthermal phase change, plastically deformed the top layer and/or the two layers detached at the (first or the second) interface due to the intense laser interaction, and the top layer(s) buckled as it was (they were) released from high compressive stress found on as deposited IBS films [11]. It is well understood that  $\text{HfO}_2$  ( $E_{\text{gap}} = 5.1 - 5.4$  eV) exhibits a lower damage threshold [12] than  $\text{SiO}_2$  ( $E_{\text{gap}} = 9.1$  eV), and, therefore, also undergoes nonthermal melting and ablation [8] at comparatively lower fluences. The large fluence range of blister formation of FCP versus LP may also point towards a higher rate

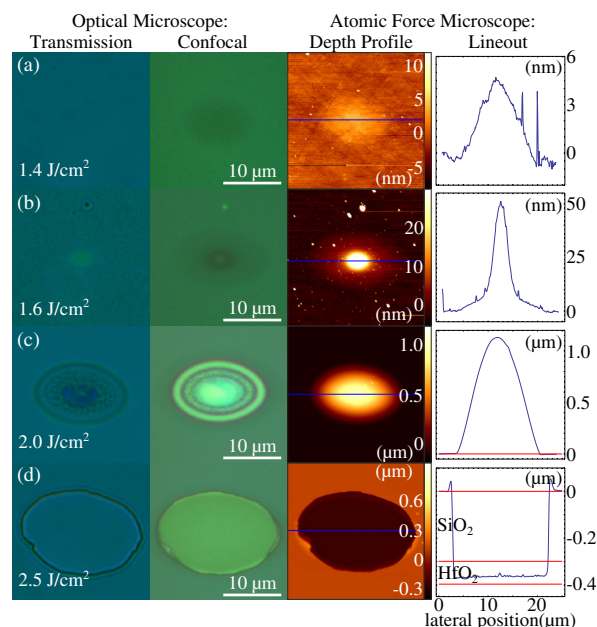


**Fig. 1.** Damage morphologies of the  $\text{HfO}_2/\text{SiO}_2$ -based double-layer sample when irradiated with a single FCP. From the left to right column, transmission and confocal optical microscope images, atomic force microscope depth profiles, and associated lineouts. From the top to bottom row, (a) bump formation, (b) transition from bump to blister, (c) blister formation, and (d) crater formation. Note the change in depth scale from (a) to (d).

of energy transfer from hot electrons to the lattice, as alluded before. As explained in Ref. [6], the transition from bump to blister morphology is not smooth, implying that blister formation is associated with the expansion of a high pressure gas or liquid–gas mixture [as evidenced by the presence of microvoids [13,14] inside some blisters, e.g., Fig. 1(c) left-most panel] of  $\text{HfO}_2$ , assuming that the  $\text{HfO}_2$  layer absorbs most of the pulse energy that leads to damage.

The smallness of energy absorbed by the  $\text{SiO}_2$  layer compared to that in the  $\text{HfO}_2$  layer can be partially justified by comparing the laser-induced damage threshold (LIDT) fluences of the multilayer samples to that of the single-layer QWOT  $\text{HfO}_2$  sample. Absorption of the  $\text{SiO}_2$  layer may be more significant for higher fluences, which will be discussed in the next section. The damage probability method was used to measure the LIDT fluences, where the fluence threshold is defined as the highest fluence for which the probability of damage is zero. Damage is defined as bump formation, which is visible under a confocal optical microscope [Fig. 1(a)]. The FCP LIDT fluences for the single-layer QWOT  $\text{HfO}_2$ , double-layer samples, and quad-layer samples are  $0.8 \pm 0.08$ ,  $0.85 \pm 0.085$ , and  $0.9 \pm 0.09$   $\text{J}/\text{cm}^2$ , respectively. Within experimental uncertainty, the LIDT fluences are roughly the same, showing that the absorption of the  $\text{SiO}_2$  layer for fluences near the damage threshold is negligible to good approximation. Furthermore, our previous work showed that the FCP LIDT in fused silica is  $1.8 \pm 0.2$   $\text{J}/\text{cm}^2$  [15].

Figure 1(d) shows that for even larger fluences, the blister breaks and leaves a crater behind. As depicted in the AFM lineout, the craters are never deeper than the first two layers of the sample (for both double- and quad-layer samples). In fact, the first  $\text{HfO}_2$  layer is never entirely removed for single-shot

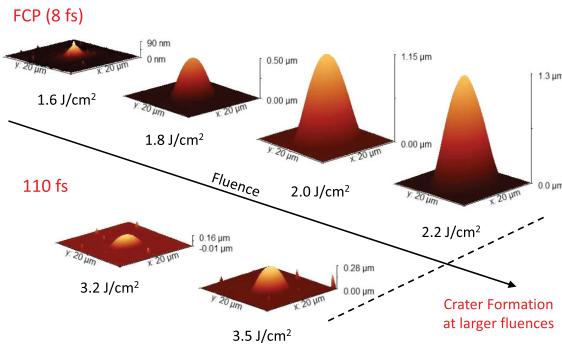


**Fig. 2.** 3D blister AFM profiles versus peak beam-normal fluences for double-layer samples created by single 8 fs (top) and 110 fs (bottom) pulses.

irradiation. This can be explained by the strong attenuation of the pulse due to the high density (free-carrier density,  $n_e \gtrsim 10^{21} \text{ cm}^{-3}$ ) plasma it generates, which prevents a significant amount of absorption to occur in deeper layers [5]. Despite the fact that the intensity profile of the focal spot of the beam is well-approximated by a Gaussian profile, the AFM lineout in Fig. 1(d) shows that the depth profile of the bottom of the crater is relatively flat. Also, the crater edges are extremely steep, which is why they look so dark under optical microscope. Craters with flat bottoms have been observed in bulk solids [4,16], and have been explained by the strong increase in reflectivity and absorption of the laser-generated plasma for the center of the beam where the intensity is the largest [17]. In the case of thin film samples, it is likely that the distribution of energy deposition within the thin film depends on the interplay between thin film interference and plasma attenuation [5,6].

We have observed significant difference in dynamics, damage threshold, and morphology of damage sites induced by FCP versus those caused by LP. Such pulse duration comparison of damage site morphology as a function of incident

fluence was presented in detail in Fig. 5 of Ref. [6]. Briefly, the blister/damage threshold fluence for FCPs is roughly half that for LP, and the range of blister-forming fluences is significantly larger for FCPs than for LP, as also shown in Fig. 2. In the current paper, we primarily concentrate on pulse duration variation of the dynamics of ablation of these films, as shown via the TRSM images in Fig. 3, from 2 to 8 ns (first six columns) and at 20 and 46 ns (last two columns) for both samples and both pulse durations. The quad-layer sample is shown in Figs. 3(a) and 3(b), and the double-layer sample is shown in Figs. 3(c) and 3(d). From 2–3 ns, concentric fringes (Newton's rings [5,18]) are more clearly observed for FCP craters [Figs. 3(a) and 3(c)] than for 110 fs craters, where faint outlines of outer fringes seem to appear until the 2.5 ns frame, obscured due to an overall lower probe transmission. After that for LP, they disappear (or are obscured) completely. As mentioned previously, these fringes are due to the variation of the interference condition of the sample as the blister expands. These observations seem to point toward two different ablation mechanisms, one (photomechanical spallation, or PM) favored by FCP while the other (phase explosion, or PE) favored by LP. Typically, PM [19] happens just above the ablation threshold, where a top layer of an ultrafast laser excited region begins to expand into vacuum (time scale  $\sim 250 \text{ ps}$  [13]) to release high compressive stress before the equilibration of nonthermal electrons with phonons. This expansion causes the layer beneath it to be under high tensile stress, and the resultant rarefaction wave traveling deeper into the nonthermal melt zone (requiring  $\sim 7\%$  valence electron excitation into the conduction band [20]), nucleating and expanding voids. As the laser fluence is increased, with faster expansion speed, the temperature of the thermally isolated spalled layer keeps increasing while its thickness decreases. At a certain extrapolated temperature, the spalled layer thickness reduces to zero, where the liquid and vapor phase explosively (PE) separate under the initial compressive pressure [13]. Due to the existence of large distribution of atomic to high temperature

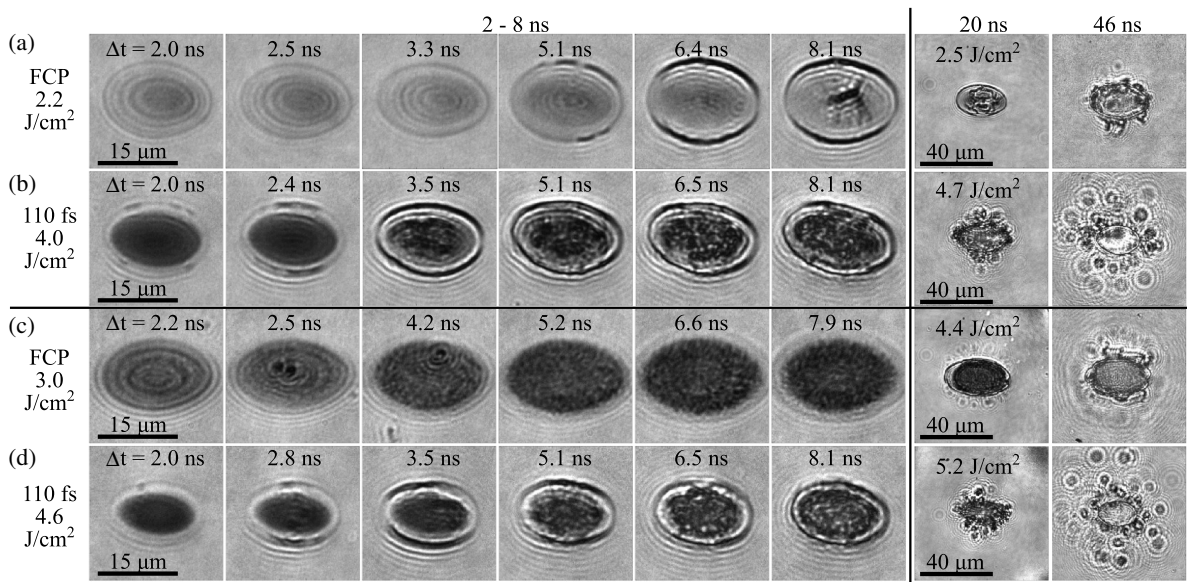


**Fig. 3.** Time-resolved surface microscopy (TRSM) images of ablation dynamics from 2–8 ns (first six columns) and at 20 and 46 ns (last two columns). (a) and (b) correspond to FCP and 110 fs pulse ablation, respectively, on the quad-layer sample; (c) and (d) correspond to FCP and 110 fs pulse ablation on the double-layer sample. Note the change in scale for the 20 and 46 ns images.



nano-droplets [13] in a PE region, it is expected that light transmission through the region would be drastically reduced, due to both scattering and absorption. We believe that Figs. 3(b) and 3(d) clearly show the evidence of PE for LP, whereas Figs. 3(a) to 3(c) exhibit a transition from PM to PE for FCP. The presence of layers and interfaces may further complicate our analysis here, especially how ballistic electron transport and electron–phonon coupling parameters may drastically change due to a small change in interface [21] (e.g., the second  $\text{HfO}_2$ – $\text{SiO}_2$  interface difference between bi- and quad-layer samples, where the  $\text{SiO}_2$  is as deposited versus substrate, respectively).

The borders near the top and bottom of the elliptical irradiated zone for 110 fs craters begin to darken at 2.0 ns for the quad-layer sample [Fig. 3(b)] and 2.8 ns for the double-layer sample [Fig. 3(d)], and the darkening propagates towards the sides [e.g., 2.8 and 3.5 ns frames in Fig. 3(d)]. This is most likely due to the mechanical failure of the top layer from the high pressure expansion of the  $\text{HfO}_2$  layer below, and the higher stress along the minor axis of the elliptically shaped sites causes the failure to initiate along the top and bottom. The onset of mechanical failure for FCP-generated craters on the quad-layer sample occurs much later [5.1 ns, Fig. 3(a)], and the 20 and 46 ns images for LP [last two frames in Figs. 3(b) and 3(d)] show many more small fragments being ejected away from the crater than for FCPs, as if the top layer shatters more violently for longer pulses. Although large scale 3D molecular dynamic-type simulations for laser damage at present cannot extend to multiple ns time scale [13], the stronger explosive expansion of debris field does point toward PE as the dominant mechanism for LP ablation shown in Figs. 3(b) and 3(d).

A 1D dynamic FDTD model [5] of the samples (thickness adjusted for angle of incidence) with Keldysh ionization (no collisional ionization) integrated over FCP and LP reveals that peaks of free electron density are governed by interference antinodes, existing in the middle of the top  $\text{SiO}_2$  layer and at the second interface between the (second)  $\text{HfO}_2$  layer and the third  $\text{SiO}_2$  layer (or substrate for the bilayer sample). For the quad-layer sample, peak  $n_e$  in layers 1 and 2 are 36% and 50% of the valence band density for FCP (peak fluence  $2.2 \text{ J/cm}^2$ ), whereas for LP, they are 3.6% and 10% (peak fluence  $4.0 \text{ J/cm}^2$ ), respectively. The results imply that for both FCP and LP, the  $\text{HfO}_2$  layer is sufficiently excited to undergo nonthermal phase change, and the  $\text{SiO}_2$  layer may be absorbing a significant amount of energy when irradiated with FCPs, but not with LP. Therefore, it is possible that the transient temperature and dynamic mechanical properties of the FCP excited top layer are different than for those of LP. Closer to the melting point, the top layer would most likely plastically deform over a much larger range of strains before reaching mechanical failure and breaking, which could explain why the onset time of mechanical failure for FCPs is later than for LP. This could also partially explain why the blister-forming fluence range and volume expansion are significantly larger for FCP than for LP (see Fig. 2). Similar results were obtained from bilayer sample simulations, albeit the peak free-carrier densities in respective layers were  $\sim 50\%$  smaller due to lower field intensification in the layers.

The pulse duration dependence of single-shot, LIDA of double- and quad-layer  $\text{HfO}_2/\text{SiO}_2$ -based thin film samples was studied down to the FCP regime using *ex situ* imaging as well as *in situ* TRSM. Both samples exhibited a novel, blister-like morphology for a range of fluences between the damage

and crater-forming thresholds, and scaling the blister size with incident fluence was found to significantly depend on the pulse duration. The TRSM images show dramatic differences in the ablation dynamics between FCPs and LPs. For FCPs, the evolution of the blister morphology before a crater is formed is observable through concentric interference fringes, which are obscured for LPs by a much lower probe transmission. At long delay times, LPs result in crater formation that appears qualitatively more explosive than for the case of FCPs. Our findings point toward inherent differences in the energy deposition dynamics between the two pulse durations, and also underline the need for multiphysics approaches to modeling such as those found in Ref. [22].

**Funding.** Air Force Office of Scientific Research (FA9550-16-1-0069); UES Inc. (S-136-030-002/FA8650-17-D-5407); Office of Naval Research (N00014-17-1-2536); Office of Science (STTR DE-DE-SC0019900).

**Acknowledgment.** The authors also acknowledge valuable discussions with Vitaly Gruzdev and Simin Zhang.

**Disclosures.** The authors declare no conflicts of interest.

## REFERENCES

1. V. Gruzdev and O. Sergaeva, *Phys. Rev. B* **98**, 115202 (2018).
2. S. K. Sundaram and E. Mazur, *Nat. Mater.* **1**, 217 (2002).
3. B. Chimier, O. Utéza, N. Sanner, M. Sentis, T. Itina, P. Lassonde, F. Légaré, F. Vidal, and J. C. Kieffer, *Phys. Rev. B* **84**, 094104 (2011).
4. M. Lenzen, *Int. J. Modern Phys. B* **13**, 1559 (1999).
5. N. Talisa and E. Chowdhury, *Opt. Express* **26**, 30371 (2018).
6. N. Talisa, M. Tripepi, B. Harris, A. AlShafey, J. Krebs, A. Davenport, E. Randel, C. S. Menoni, and E. A. Chowdhury, *Proc. SPIE* **11173**, 38 (2019).
7. M. C. Downer, R. L. Fork, and C. V. Shank, *J. Opt. Soc. Am. B* **2**, 595 (1985).
8. J. Bonse, G. Bachelier, J. Siegel, and J. Solis, *Phys. Rev. B* **74**, 134106 (2006).
9. N. Šiaulytis, L. Gallais, and A. Melninkaitis, *Opt. Lett.* **39**, 2164 (2014).
10. B. Langdon, D. Patel, E. Krous, J. J. Rocca, C. S. Menoni, F. Tomasel, S. Kholi, P. R. McCurdy, P. Langston, and A. Ogloza, *Proc. SPIE* **6720**, 321 (2008).
11. B. Pond, J. DeBar, C. Carniglia, and T. Raj, *Appl. Opt.* **28**, 2800 (1989).
12. M. Mero, J. Liu, W. Rudolph, D. Ristau, and K. Starke, *Phys. Rev. B* **71**, 115109 (2005).
13. C. Wu and L. V. Zhigilei, *Appl. Phys. A* **114**, 11 (2014).
14. S. I. Ashtikov, N. A. Inogamov, V. V. Zhakhovskii, M. B. Agranat, I. I. Oleinik, S. I. Anisimov, and V. E. Fortov, *J. Exp. Theor. Phys. Lett.* **95**, 176 (2012).
15. K. R. P. Kafka, N. Talisa, G. Tempea, D. R. Austin, C. Neacsu, and E. A. Chowdhury, *Opt. Express* **24**, 28858 (2016).
16. J. Bonse, M. Munz, and H. Sturm, *IEEE Trans. Nanotechnol.* **3**, 358 (2004).
17. L. Jiang and H. L. Tsai, *J. Appl. Phys.* **104**, 093101 (2008).
18. J. P. McDonald, J. A. Nees, and S. M. Yalisove, *J. Appl. Phys.* **102**, 063109 (2007).
19. E. Leveugle, D. S. Ivanov, and L. V. Zhigilei, *Appl. Phys. A* **79**, 1643 (2004).
20. D. R. Austin, K. R. P. Kafka, Y. H. Lai, Z. Wang, C. I. Blaga, and E. A. Chowdhury, *Opt. Lett.* **43**, 3702 (2018).
21. A. Giri, J. T. Gaskins, B. F. Donovan, C. Szejewski, R. J. Warzoha, M. A. Rodriguez, J. Ihlefeld, and P. E. Hopkins, *J. Appl. Phys.* **117**, 105105 (2015).
22. S. M. Gracewski, S. Boylan, J. C. Lambropoulos, J. B. Oliver, T. J. Kessler, and S. G. Demos, *Opt. Express* **26**, 18412 (2018).